Roverato, Enrico; Kosunen, Marko; Lemberg, Jerry; Stadius, Kari; Ryynänen, Jussi

RX-Band Noise Reduction in All-Digital Transmitters With Configurable Spectral Shaping of Quantization and Mismatch Errors

Published in:
IEEE TRANSACTIONS ON CIRCUITS AND SYSTEMS I-REGULAR PAPERS

DOI:
10.1109/TCSI.2014.2335012

Published: 01/01/2014

Document Version
Peer reviewed version

Please cite the original version:
Roverato, E., Kosunen, M., Lemberg, J., Stadius, K., & Ryynänen, J. (2014). RX-Band Noise Reduction in All-Digital Transmitters With Configurable Spectral Shaping of Quantization and Mismatch Errors. *IEEE TRANSACTIONS ON CIRCUITS AND SYSTEMS I-REGULAR PAPERS*, *61*(11), 3256-3265.
https://doi.org/10.1109/TCSI.2014.2335012

RX-band Noise Reduction in All-Digital Transmitters with Configurable Spectral Shaping of Quantization and Mismatch Errors

Enrico Roverato, *Student Member, IEEE,* Marko Kosunen, *Member, IEEE,* Jerry Lemberg, Kari Stadius, *Member, IEEE,* and Jussi Ryynänen, *Member, IEEE*

***Abstract*—This paper describes the first purely digital approach to reduce the receive band noise in digitally-intensive RF transmitters. The proposed solution applies bandpass delta-sigma modulation and dynamic element matching (DEM) to the receive band (RX-band) instead of the transmit band. This enables selective attenuation of the noise originating from amplitude quantization and static mismatches of the digital-to-analog converter (DAC), which would otherwise reach the transmitter output almost unattenuated. A highly configurable 4^{th}-order noise transfer function is designed to achieve optimum attenuation in the programmable RX-band, while ensuring negligible degradation of the transmitted signal quality as well as stable operation of the tree structure DEM encoder. A general validation of DEM, independent from the duration of the DAC impulse response, is also presented. The proposed solution is verified through system-level simulations with LTE signals. In the presence of typical amplitude and timing mismatches, the RX-band noise can be reduced below –160 dBc/Hz without filtering after the DAC, thus potentially enabling SAW-less operation of all-digital transmitters.**

***Index Terms*—All-digital transmitter, RX-band noise, bandpass delta-sigma modulation, dynamic element matching (DEM), mismatch shaping, programmable noise transfer function (NTF).**

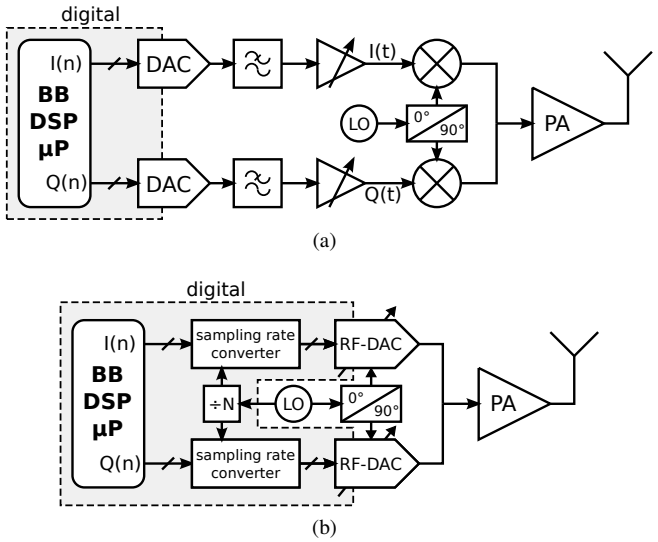

Fig. 1. (a) Direct conversion transmitter architecture. (b) Direct-digital RF-modulator (DDRM) transmitter architecture [3]–[5].

I. Introduction

During the last 15 years, the trend in the design of radio-frequency (RF) integrated circuits (ICs) has been to move from analog to digital and mixed-signal circuit solutions [1]–[11]. The main reasons behind this change come from the increasing transmission bandwidth and flexibility needed in modern wireless communication systems, as well as the continuous development of sub-micron CMOS technologies. The ultimate target of this digitalization trend is the so-called "all-digital radio transceiver", where most of the RF functions are performed by digital circuits, and the interface with the analog domain is located just in front of the antenna.

In the context of radio transmitters, digitalization started first with digital baseband modulators [1], [2]. However, the first true effort towards an all-digital solution is the direct-digital RF-modulator (DDRM) [3]–[5]. Fig. 1 compares the DDRM with the classical direct-conversion transmitter. In the DDRM, the digital-to-analog converter (DAC) and upconverting mixer are combined into a single circuit block, also known as RF-DAC. This combination is enabled by the increasing speed of modern CMOS processes, which allows to interpolate the baseband signal to very high sampling rates in the digital domain. As a consequence, the analog reconstruction filter after the DAC is no longer needed, because the digital images are located far enough from the transmitting band, where they are highly attenuated by the *sinc* response of the converter's zero-order hold.

In frequency-division duplexing (FDD) systems, the transmitter (TX) and the receiver (RX) are usually constrained to share the same antenna. Because of limited duplexer isolation, an excess of transmit power leaking to the receive band (RX-band) can interfere with the reception of weak signals, thus degrading the receiver sensitivity. The TX-RX isolation can be boosted through the use of Surface Acoustic Wave (SAW) filters. These filters are bulky, expensive, and their frequency response is fixed, which is very undesirable in the context of increasing flexibility demand.

Digitally-intensive TX architectures (like the one shown in Fig. 1(b)) tend to make this interference problem even worse. Because there is no analog reconstruction filter after the DAC, the quantization noise reaches the TX output almost

Manuscript received March 1, 2014; revised May 8, 2014; accepted May 22, 2014. Date of publication July 99, 2099; date of current version October 99, 2099. This paper was recommended by Associate Editor Pui-In Mak.

The authors are with the Department of Micro- and Nanosciences, Aalto University School of Electrical Engineering, 02150 Espoo, Finland (e-mail: enrico.roverato@aalto.fi).

Digital Object Identifier 0000000000000000000

unattenuated. Theoretically, the problem could be straightforwardly solved by increasing the effective number of bits (ENOB) of the converter [5]. However, the maximum ENOB that can be achieved without calibration is typically around 10-12 bits, which is not sufficient to meet the tight RX-band noise requirement [6]. Hence, such a solution is controversial to the objectives of digital RF, i.e. simplification of the analog part and relaxation of its performance requirements.

Recently, a few alternative methods have been proposed to reduce the out-of-band quantization noise of digital-like TX architectures. For example, the concept of semi-digital finite impulse response (FIR) filtering was demonstrated in [7] for single-bit, and in [8], [9] for multibit RF-DACs. This approach consists of connecting many converters with different weights in a FIR-like configuration, in order to reduce the quantization noise floor at a programmable distance from the main channel. Because the filter coefficients are implemented by means of tunable current sources, the design of this circuit is essentially analog, and the maximum achievable performance is thus limited by mismatches among different converters. Other techniques to improve the resolution of the amplitude path of all-digital polar transmitters, thus decreasing the out-of-band noise, are presented in [10], [11]. However, these methods cannot be fully implemented within DSP, as they make use of e.g. adaptive predistortion and variable delay chains.

This paper describes the first ever purely digital approach to alleviate the problem. Purely digital methods benefit more of CMOS process evolution, and are therefore preferable over the semi-digital approaches discussed above. The method presented here exploits tunable bandpass $\Delta\Sigma$ modulation to push the quantization noise outside the programmable RX-band, instead of the main signal band [12]–[18]. Dynamic element matching (DEM) is similarly used to shape the noise originating from amplitude and timing mismatches of the DAC, that would otherwise degrade the maximum achievable performance [19]–[26]. In order to perform highly tunable noise shaping, a flexible 4$^{\text{th}}$-order noise transfer function (NTF) is developed, with emphasis on pole placement. The designed NTF achieves optimum attenuation in the programmable RX-band, while ensuring negligible degradation of the transmitted signal quality as well as stable operation of the tree structure DEM encoder. Moreover, this paper extends the existing theory on DEM with a more general analysis, which is independent from the duration of the DAC impulse response. The robustness of the proposed approach in the presence of realistic amplitude and timing DAC mismatches is accurately verified through system-level simulations, performed with Long Term Evolution (LTE) signals in a number of different channel configurations and mismatch scenarios.

The paper is organized as follows. Section II introduces bandpass $\Delta\Sigma$ modulation, illustrates the proposed NTF design method, and shows that simple noise shaping is not sufficient to solve the out-of-band noise challenge in the presence of mismatch induced DAC nonlinearities. Section III reviews and extends the theory of DEM from a signal processing perspective. Various system-level simulations to demonstrate the effectiveness of the proposed method are presented in Section IV. Finally, Section V concludes the paper.

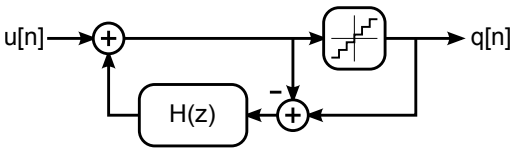

Fig. 2. Error-feedback $\Delta\Sigma$ modulator.

II. Tunable Bandpass $\Delta\Sigma$ Modulation

$\Delta\Sigma$ modulation is an established and effective technique to enhance the linearity of analog-to-digital and digital-to-analog data converters [12]–[18]. The main idea behind $\Delta\Sigma$ modulation is to connect an amplitude quantizer in a properly designed feedback loop, which enables the spectral density of the quantization error (resulting from the quantizer's finite resolution) to be shaped according to a predetermined noise transfer function (NTF). Traditionally, the noise shaping capabilities of $\Delta\Sigma$ modulation have been exploited in data conversion applications, to augment the converter's signal-to-noise ratio (SNR) in the frequency band occupied by the main signal. In this paper, we explore the possibility to use $\Delta\Sigma$ modulation to remove the quantization noise from the RX-band, which is located at a programmable distance from the main signal band.

A wide variety of loop architectures can be used to implement $\Delta\Sigma$ DACs [12]. Among them, one of the simplest and hence most attractive is the error-feedback (EF) structure (Fig. 2). In this architecture, the quantization error is evaluated by subtracting the quantizer input from its output, and it is then fed back to the input through the loop filter $H(z)$. If the quantizer is replaced by its linear model, consisting of additive random white uniformly-distributed quantization noise $e[n]$, linear analysis results in

$$Q(z) = U(z) + \big(1 + H(z)\big)E(z), \tag{1}$$

where $Q(z)$, $U(z)$ and $E(z)$ are the z-transforms of the modulator output, input and quantization error respectively. Therefore, the modulator output contains a replica of the input signal, i.e. the signal transfer function (STF) is unity. Furthermore, the noise transfer function is given by

$$\text{NTF}(z) = 1 + H(z). \tag{2}$$

Hence, the spectral properties of the noise appearing at the modulator output can be altered by properly designing the loop filter $H(z)$.

The feedback loop in Fig. 2 is physically realizable only if there is at least one delay between the input and the output of the loop filter. It can be demonstrated that this requirement translates into the important NTF realizability condition

$$\text{NTF}(z) = \frac{1 + \sum_{i=1}^{N} b_i z^{-i}}{1 + \sum_{i=1}^{N} a_i z^{-i}}, \tag{3}$$

where N is the modulator order, and $\{b_i, a_i\}$ is the set of NTF coefficients [12].

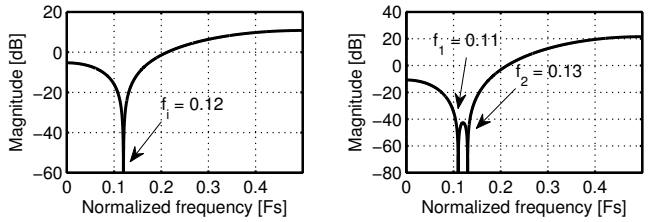

(a) (b)

Fig. 3. (a) Frequency response of a digital single-notch filter, with $\omega_i = 2\pi f_i$. (b) Frequency response of the cascade of two single-notch filters.

A. NTF Design

The topic of NTF design is thoroughly treated in the literature on $\Delta\Sigma$ modulation [12]–[17]. However, very little can be found regarding the design of a highly tunable NTF in the discrete-time domain. One example is the method adopted in [18], which uses the discrete-time lowpass-to-bandpass transformation to shift a prototype lowpass NTF to a programmable center frequency. In this paper, we describe how to design a tunable NTF by directly placing the poles and zeros on the z-plane, thus giving more insight into the synthesis process.

The RX-band noise reduction technique proposed in this paper assumes that the quantizer resolution is large enough to represent the transmitted signal with sufficient performance overhead, but too low to achieve the RX-band noise requirement. This allows to design the NTF for noise removal only from the RX-band, as long as the NTF gain in the transmit band is less than the SNR overhead. In addition, because the EF structure has STF $= 1$, the transmitted signal is not affected by the shape of the NTF.

In order to attenuate the quantization noise in the RX-band, the NTF must contain at least one programmable zero. In the z-domain, the function

$$N_i(z) = 1 - (2\cos\omega_i)z^{-1} + z^{-2} \tag{4}$$

realizes a digital notch filter (Fig. 3(a)), where the position of the zero ω_i can be programmed over the whole Nyquist range $[0, \pi]$ by adjusting the coefficient of z^{-1}. By cascading several such single-notch filters, attenuation can be provided over a wider range of frequencies. For example, Fig. 3(b) shows the frequency response of the filter given by

$$N(z) = N_1(z) \cdot N_2(z), \tag{5}$$

where the two single-notch transfer functions $N_1(z)$ and $N_2(z)$ (each defined as in (4)) create two slightly displaced zeros at frequencies ω_1 and ω_2 respectively. It can be immediately verified that the cascade of any number of single-notch filters fulfills the realizability condition given by (3).

If we choose (5) as our candidate NTF, an obvious question concerns the optimal zero location, that minimizes the total noise power over the RX-band. Since the quantization noise was assumed to be white, this problem is equivalent to minimizing the integral of the squared magnitude of $N(e^{j\omega})$ over the same band, expressed by the function

$$I(\omega_1, \omega_2) = \int_{\omega_0 - \frac{\omega_R}{2}}^{\omega_0 + \frac{\omega_R}{2}} \left| N_1(e^{j\omega}) \cdot N_2(e^{j\omega}) \right|^2 d\omega, \tag{6}$$

where ω_0 and ω_R are the center and the width of the RX-band respectively [12], [13]. The above integral can be solved in closed form under the following simplifying assumptions:

- the two zeros ω_1 and ω_2 are equidistant from the RX-band center (that is, they are located at $\omega_0 \pm \omega_Z$), and
- the relationship $\omega_R \ll \omega_0$ holds, allowing the squared magnitude of each single notch function $N_i(e^{j\omega})$ to be approximated around ω_i as

$$\begin{aligned} \left|N_i(e^{j\omega})\right|^2 &= \left|1 - (2\cos\omega_i)e^{-j\omega} + e^{-j2\omega}\right|^2 \\ &= \left|(1 - e^{-j(\omega_i+\omega)}) \cdot (1 - e^{j(\omega_i-\omega)})\right|^2 \\ &\approx \left|(1 - e^{-j2\omega_i})\right|^2 \cdot \left|j(\omega - \omega_i)\right|^2 \\ &= \kappa_i(\omega - \omega_i)^2, \end{aligned} \tag{7}$$

where $\kappa_i \triangleq \left|(1 - e^{-j2\omega_i})\right|^2$ is a constant. The optimal zero location is found by setting

$$\frac{d}{d\omega_Z} I(\omega_0 + \omega_Z, \omega_0 - \omega_Z) = 0, \tag{8}$$

which yields

$$\omega_Z = \frac{\omega_R}{2\sqrt{3}}. \tag{9}$$

In practice, an EF $\Delta\Sigma$ modulator with NTF given by (5) can be implemented with extremely low complexity. Our synthesis results in a 28nm CMOS process show that the system can be realized with less than 2000 gates, it works at least up to 1 GHz clock frequency (worst case corner), and consumes about 2000 μm^2 silicon area and 1.5 mW power. These results were obtained for a modulator with 8-bit quantizer implemented in fixed-point arithmetic. The wordlengths of input signal $u[n]$ and programmable NTF coefficients were chosen to be 15 and 8 bits respectively, which are sufficient to achieve low round-off noise and fine tuning resolution.

Fig. 3(b) shows that the filter $N(z)$ provides good attenuation around ω_1 and ω_2, but the gain increases rapidly outside the stopband, up to a maximum exceeding 20 dB. This translates into large quantization noise amplification outside the RX-band, which may cause degradation of the transmitted signal quality, as well as violation of the spectral mask requirements of some radio standards. In order to reduce the out-of-band filter gain, the poles of the transfer function must be moved away from the point $z = 0$, closer to the zeros.

The poles of the NTF are usually arranged in a Butterworth or Chebyshev configuration [12]–[17]. However, due to the high range of tunability needed in our application, here we follow a more intuitive and flexible approach. The concept is illustrated in Fig. 4(a). The basic idea is to place each pole at the same angle of the corresponding zero, on a circle of radius $r < 1$ (necessary stability condition). As r approaches 1, the poles approach the zeros, resulting in more effective zero/pole compensation that reduces the out-of-band gain of the filter. Correct pole placement is achieved by modifying (5) into

$$R(z) = \frac{N(z)}{D(z)} = \frac{N_1(z) \cdot N_2(z)}{D_1(z) \cdot D_2(z)}, \tag{10}$$

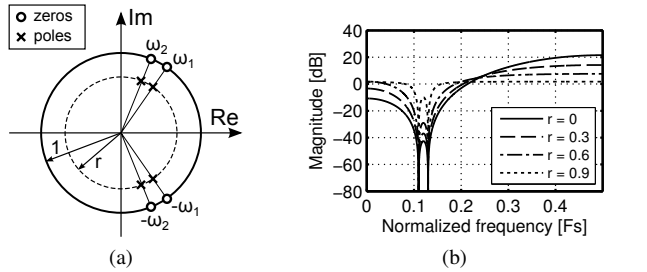

(a) (b)

Fig. 4. Illustration of the proposed out-of-band gain reduction approach for a double-notch digital filter. (a) Placement of zeros and poles in the z-plane. (b) Frequency response for $f_1 = 0.11$, $f_2 = 0.13$, and different values of r.

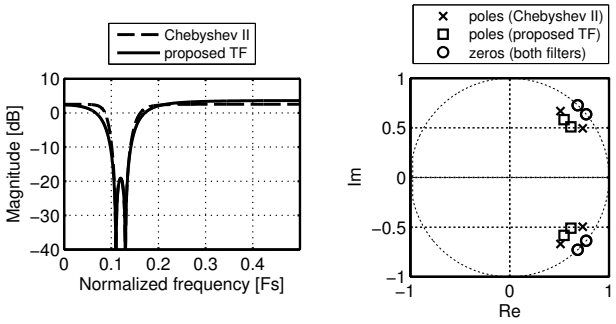

(a) (b)

Fig. 5. Comparison between the proposed transfer function (with $f_1 = 0.11$, $f_2 = 0.13$, $r = 0.8$) and a 4$^{\text{th}}$-order Chebyshev filter of the second kind with the same zero location and stopband ripple. (a) Frequency responses. (b) Location of zeros and poles.

where the $N_i(z)$ factors are still given by (4), while each $D_i(z)$ term is in the form

$$D_i(z) = 1 - (2r\cos\omega_i)z^{-1} + r^2 z^{-2}. \tag{11}$$

Note that the modified transfer function still satisfies (3).

Fig. 4(b) shows the frequency response of (10) for different values of r. Although the out-of-band filter gain is effectively reduced as r approaches 1, an increasing sharpness of the two notches around ω_1 and ω_2 is also observed. The net effect is a degradation of the average stopband attenuation performance of the filter. Thus, the parameter r can be used to trade-off the levels of the quantization noise floor inside and outside the RX-band.

Fig. 5 compares (10) with a classical 4$^{\text{th}}$-order Chebyshev filter of the second kind, designed to achieve the same zero location and stopband ripple (and properly scaled as to fulfill (3)). It can be seen that the two transfer functions yield a comparable performance. Thus, we finally select (10) as the NTF for our $\Delta\Sigma$ modulator, as it enables the additional flexibility to use very simple closed form expressions for filter coefficient calculation. The optimal zero location is still given by (9), provided that the denominator of the NTF is approximately constant over the entire RX-band. This condition holds well for values of r up to about 0.9.

B. Sensitivity to DAC Mismatches

A preliminary system-level simulation was performed, in order to evaluate the effectiveness and feasibility of $\Delta\Sigma$ modulation for RX-band noise removal. In the simulation, a 20 MHz LTE signal (with sampling rate $f_s = 983$ MHz) is fed to the cascade of a $\Delta\Sigma$ modulator and a 10-bit DAC. No upconversion to RF is performed at this point. The RX-band center frequency is located at 190 MHz offset from the main signal band, which is the duplex distance used in E-UTRA Band 1 [27]. The target average noise floor level in the RX-band is –160 dBc/Hz [5], [28].

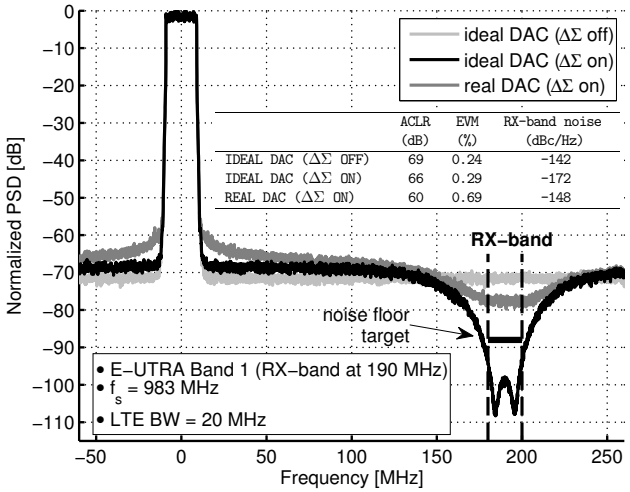

Fig. 6. System-level simulation performed to assess the effectiveness of $\Delta\Sigma$ modulation for RX-band noise removal. The plot shows the spectra at the output of an ideal 10-bit DAC (with and without $\Delta\Sigma$ modulation), and a real 10-bit DAC with static amplitude mismatch $\sigma_{LSB} = 3\%$.

The 10-bit DAC was modeled as an array of conversion cells. The function of each cell is to convert to analog a single 1-bit signal $b_i[n]$ from the digital circuitry. In the discrete-time domain, the cell output is given by

$$y_i[n] = \begin{cases} K_i \frac{\Delta}{2} + \varepsilon_i & \text{if } b_i[n] = 1 \\ -(K_i \frac{\Delta}{2} + \varepsilon_i) & \text{if } b_i[n] = 0, \end{cases} \tag{12}$$

where Δ is the DAC's minimum step size, K_i is the weight of the conversion cell, and ε_i models the inevitable amplitude error due to CMOS process variations. The two output values are assumed to be symmetrical because of differential implementation. The conversion cell array is split into a 6-bit binary-coded Least Significant Bit (LSB) segment, and a 4-bit thermometer-coded Most Significant Bit (MSB) segment. The amplitude error of each cell is independently taken from a Gaussian distribution with zero mean and standard deviation

$$\sigma(\varepsilon_i) = \sigma_{LSB} \cdot \sqrt{K_i}, \tag{13}$$

where σ_{LSB} is the reference deviation in the LSB cell (with weight 1). This expression is justified by the fact that a cell with weight $K_i > 1$ can be thought as the sum of K_i cells with weight 1, driven by the same 1-bit signal.

The simulation results are displayed in Fig. 6. The black line is the spectrum at the output of the ideal DAC (with $\sigma_{LSB} = 0$). The $\Delta\Sigma$ modulator implements the NTF given by (10) through the EF structure of Fig. 2. For reference, the spectrum with no $\Delta\Sigma$ modulation (i.e. uniform quantization only) is also shown in Fig. 6. In both cases, the chosen

resolution of 10 bits provides excellent transmitted signal quality, as measured by the Error Vector Magnitude (EVM) and Adjacent Channel Leakage Ratio (ACLR) [27], [28]. However, the average RX-band noise can be reduced below the target level only through $\Delta\Sigma$ modulation, reaching a theoretical value of –172 dBc/Hz. The pole radius of 0.8 keeps the maximum NTF gain around 3 dB, thus ensuring a negligible ACLR and EVM penalty compared to the case with no $\Delta\Sigma$ modulation.

The dark gray line in Fig. 6 is the spectrum of the DAC output, when $\sigma_{LSB} = 3\%$ relative to Δ. The shown curve was obtained from a single simulation run, since the small variation that can be observed when using different sets of randomly generated static mismatches is irrelevant at this point. Despite the high-order nonlinearity resulting from amplitude errors, the EVM and ACLR of the transmitted signal undergo only a slight degradation, which still leaves a large margin to LTE specifications. However, the notch at the RX-band is almost totally "filled", with the noise floor degrading to –148 dBc/Hz.

The reason for this performance degradation lies in the reconstruction mechanism of the analog signal at the DAC output. Even though the spectral density of the digital input is effectively shaped by the $\Delta\Sigma$ modulator, all the $b_i[n]$ signals driving each conversion cell show a nearly white spectrum, as they have little or no correlation with the input. Therefore, if the recombination of these 1-bit signals is not exact, their spectra will leak to the DAC output. The resulting "mismatch noise" will fill the notch at the RX-band, thus vanishing the action of the $\Delta\Sigma$ modulator.

III. Dynamic Element Matching

Dynamic element matching (DEM) denotes a set of popular techniques, that have been used to boost the linearity of multibit digital-to-analog converters for over 20 years [19]–[26]. The basic idea behind DEM is to scramble the order of the conversion cells in a DAC on a sample-by-sample basis, in order to convert the nonlinearity caused by static mismatches into pseudorandom noise. Optionally, the power density of this noise can be also spectrally shaped, a process known as mismatch error shaping. Like for $\Delta\Sigma$ modulation, in this paper we propose to apply these established techniques to improve the noise floor in the RX-band, rather than the SNR in the main signal band.

Among the various architectures that have been developed over the years to realize DEM, the tree structure encoder is highly attractive, due to its ability to implement a wide range of mismatch noise filtering profiles, as well as the ease with which the structure can be pipelined for high-speed digital implementation. The structure, shown in Fig. 7, applies to segmented DACs with unary-weighted MSBs and binary-weighted LSBs [21]–[23]. Note that each conversion cell in the LSB segment has to be duplicated, in order to create sufficient redundancy for DEM to work properly.

The tree encoder of Fig. 7 consists of a cascade of segmenting and nonsegmenting switching blocks. The function of a nonsegmenting switching block (Fig. 8(a)) is to split its

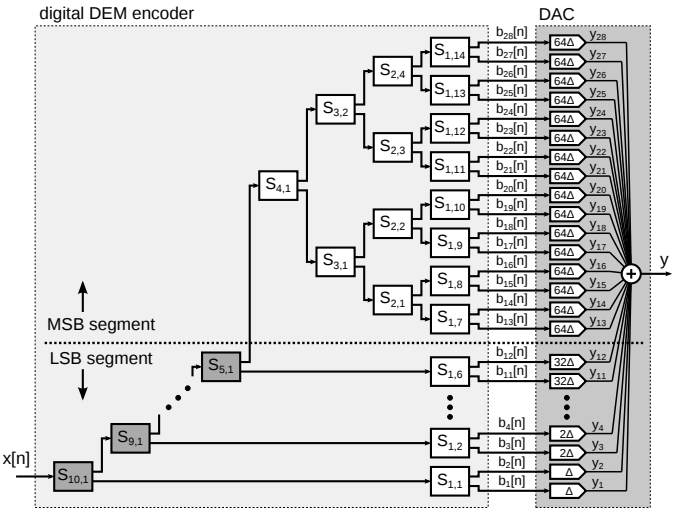

Fig. 7. Architecture of a segmented tree structure DEM encoder, driving a 10-bit DAC with 4-bit MSB segment and 6-bit LSB segment [23].

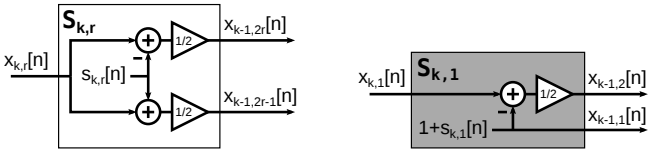

Fig. 8. Switching block architecture. (a) Nonsegmenting. (b) Segmenting.

input signal into two components, according to

$$\begin{aligned} x_{k-1,2r-1}[n] &= \frac{1}{2}\big(x_{k,r}[n] + s_{k,r}[n]\big), \\ x_{k-1,2r}[n] &= \frac{1}{2}\big(x_{k,r}[n] - s_{k,r}[n]\big), \end{aligned} \tag{14}$$

where $s_{r,k}[n]$ is a switching sequence generated within the block, which must satisfy

$$s_{k,r}[n] = \begin{cases} 0 & \text{if } x_{k,r}[n] \text{ is even} \\ \pm 1 & \text{if } x_{k,r}[n] \text{ is odd.} \end{cases} \tag{15}$$

Likewise, the outputs of a segmenting switching block (Fig. 8(b)) are given by

$$\begin{aligned} x_{k-1,1}[n] &= 1 + s_{k,1}[n], \\ x_{k-1,2}[n] &= \frac{1}{2}\big(x_{k,1}[n] - 1 - s_{k,1}[n]\big), \end{aligned} \tag{16}$$

where the switching sequence $s_{k,1}[n]$ is now constrained by

$$s_{k,1}[n] = \begin{cases} 0 & \text{if } x_{k,1}[n] \text{ is odd} \\ \pm 1 & \text{if } x_{k,1}[n] \text{ is even.} \end{cases} \tag{17}$$

The theory behind the tree structure encoder has been explained rigorously [19], [23]. The basic working principle can be intuitively understood as follows. Let $x[n]$ be the encoder input, which is a linear mapping of the $\Delta\Sigma$ modulator output to the set of nonnegative integers belonging to the encoder's maximum linear range (defined as in [23]). By applying recursively (14) and (16), it can be demonstrated that

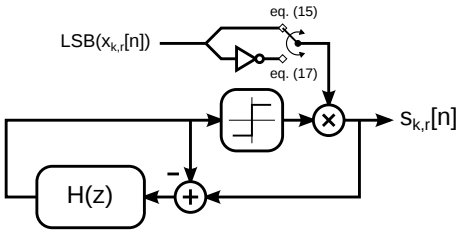

Fig. 9. Sequence generator internal to each switching block. The position of the switch depends on whether the switching block is nonsegmenting or segmenting.

each 1-bit output $b_i[n]$ can be written as

$$b_i[n] = \alpha_i \cdot x[n] + \left[\sum_{(k,r)\in P_i} \beta_{k,r} \cdot s_{k,r}[n] \right] + \gamma_i, \qquad (18)$$

where α_i, $\beta_{k,r}$ and γ_i are constants, and P_i is the set of switching block indexes found along the path from $x[n]$ to $b_i[n]$ (for example, referring to Fig. 7, $P_3 = \{(10,1),(9,1),(1,2)\}$). Therefore, if the spectral densities of all switching sequences $s_{k,r}[n]$ show a notch at the RX-band similar to that of $x[n]$, then the 1-bit outputs share the same property, due to the linear combination in (18). In addition, (14)–(17) ensure that

$$\sum_{i=1}^{M} K_i b_i[n] = x[n], \qquad (19)$$

where M is the total number of conversion cells, and K_i is the weight of the cell driven by $b_i[n]$. This constraint is known as number conservation rule.

A. Switching Sequence Generation

A block diagram of the sequence generator internal to each switching block (segmenting and nonsegmenting) is shown in Fig. 9. At the signal processing level, the structure differs from the generic EF $\Delta\Sigma$ modulator discussed in Section II only in the following:

- it has no signal input;
- the quantizer has only two output levels $\{-1,+1\}$;
- the loop includes an additional LSB multiplier.

Note that the upper input of the LSB multiplier changes whether the sequence generator belongs to a nonsegmenting or segmenting switching block. This causes either (15) or (17) to be satisfied, respectively.

With good approximation, the quantizer and multiplier together can be seen as introducing additive random error. This error is shaped by the loop, with NTF still given by (2). Furthermore, because there is no other input to the system, the output sequence consists only of the shaped error. This generation mechanism is sufficient to ensure that each $s_{k,r}[n]$ has the desired spectral properties.

From an implementation perspective, the complexity of the sequence generator (which is essentially equivalent to the EF $\Delta\Sigma$ modulator) is an important factor. Indeed, the complexity of a single switching block (Fig. 8) is largely determined by that of the sequence generator. In turn, the overall complexity of the DEM encoder is proportional to the total number of switching blocks. For example, the encoder of Fig. 7 contains 27 switching blocks, thus leading to the overall implementation complexity of 27 parallel $\Delta\Sigma$ modulators. Still, by extrapolating our synthesis results in 28nm CMOS reported in Section II, we estimate that such a DEM encoder could be realized within less than 0.1 mm^2 of silicon area, with a power consumption in the order of 50 mW.

Because the quantizer in the sequence generator has only two output levels, the $\Delta\Sigma$ loop is highly prone to instability. Even though there is no signal input, implementing the 4$^{\text{th}}$-order NTF given by (10) can easily lead to unbounded growth of the modulator's states. Fortunately, it is known that the stability of 1-bit $\Delta\Sigma$ modulators can be strengthened by reducing the maximum gain of the NTF [12]–[14]. Hence, the flexible NTF pole placement criterion discussed in Section II can be successfully exploited to stabilize the switching sequence generators. This is the key enabling factor of 4$^{\text{th}}$-order tunable DEM with a tree structure encoder. Nevertheless, the reader is reminded that there exists a trade-off between the maximum NTF gain and the average attenuation in the RX-band (Fig. 4(b)). In practice, this limits the maximum achievable performance of the DEM approach, especially with wideband signals.

B. Correction of DAC Nonlinearities

The mechanism that underlies the operation of DEM has been thoroughly explained in some good theoretical papers [23]–[26]. Here, we further extend the existing analysis with a more general validation. Because our derivation is independent from the duration of the conversion cell impulse response, the results apply to a wider class of DAC types.

Static amplitude mismatches in a DAC can be modeled as follows. In the discrete-time domain, the output $y_i[n]$ of a single conversion cell is given by

$$y_i[n] = \begin{cases} K_i \frac{\Delta}{2} + e_{hi} & \text{if } b_i[n] = 1 \\ -(K_i \frac{\Delta}{2} + e_{li}) & \text{if } b_i[n] = 0, \end{cases} \qquad (20)$$

where e_{hi} and e_{li} are the amplitude mismatch errors for the positive and negative cell state respectively. The only difference between this expression and (12) is that here e_{hi} and e_{li} are not necessarily constrained to be the same. Hence, the validity of the theory discussed in the following is not restricted to differential DAC implementations.

Equivalently, (20) can be written as

$$y_i[n] = \underbrace{K_i \Delta \left(b_i[n] - \frac{1}{2} \right)}_{y_{ID,i}[n]} + \underbrace{e_{hi} b_i[n] + e_{li}\big(b_i[n]-1\big)}_{e_{DAC,i}[n]}, \qquad (21)$$

where the ideal cell output $y_{ID,i}[n]$ and the mismatch error signal $e_{DAC,i}[n]$ are highlighted. The overall DAC output is

given by summing (21) over all M conversion cells, yielding

$$y[n] = \overbrace{\sum_{i=1}^{M} K_i \Delta\left(b_i[n] - \frac{1}{2}\right)}^{y_{ID}[n]} + \underbrace{\sum_{i=1}^{M} \Big\{ e_{hi} b_i[n] + e_{li}\big(b_i[n]-1\big) \Big\}}_{e_{DAC}[n]}, \quad (22)$$

where again the ideal DAC output $y_{ID}[n]$ and the total mismatch noise $e_{DAC}[n]$ are marked. Note that $y_{ID}[n]$ is linearly related to $x[n]$, since the $b_i[n]$ signals satisfy the number conservation rule.

As anticipated at the end of Section II, static amplitude mismatches cause the spectra of the $b_i[n]$ signals to leak to the overall DAC output $y[n]$. For a given static mismatch profile, (22) now indicates that the relation between $y[n]$ and the $b_i[n]$ signals is linear. Therefore, if DEM is implemented as described above, the spectral density of $y[n]$ will show the desired notch at the RX-band, regardless of the mismatch statistics.

The results derived above can be generalized to the continuous-time domain. It is sufficient to modify (20) to

$$y_i(t,n) = \begin{cases} u(t-nT)K_i \frac{\Delta}{2} + e_{hi}(t-nT) & \text{if } b_i[n]=1 \\ -\big(u(t-nT)K_i \frac{\Delta}{2} + e_{li}(t-nT)\big) & \text{if } b_i[n]=0, \end{cases} \quad (23)$$

where T is the sampling period, $u(t)$ is the ideal, unity-weighted impulse response of all conversion cells, and $e_{hi}(t)$ and $e_{li}(t)$ are error pulses that can now include not only amplitude mismatches, but also timing and pulse shape mismatches. This equation shows how the n-th sample of the discrete-time 1-bit driving signal $b_i[n]$ is converted to a continuous-time analog signal. The complete output signal of the conversion cell is found by convolving (23) with $b_i[n]$, leading to

$$y_i(t) = \overbrace{\sum_{n=-\infty}^{+\infty} \left\{ u(t-nT) \cdot K_i \Delta\left(b_i[n] - \frac{1}{2}\right) \right\}}^{y_{ID,i}(t)} + \underbrace{\sum_{n=-\infty}^{+\infty} \Big\{ e_{hi}(t-nT) \cdot b_i[n] + e_{li}(t-nT) \cdot \big(b_i[n]-1\big) \Big\}}_{e_{DAC,i}(t)}, \quad (24)$$

which is the equivalent continuous-time form of (21). The overall DAC output can be again found by summing (24) over all M conversion cells, yielding an expression similar to (22).

The theory presented in [23]–[26] is developed under the assumption that $u(t)$, $e_{hi}(t)$ and $e_{li}(t)$ are zero outside of $0 \leqslant t < T$. Here, it is shown that DEM works properly regardless of the shape and duration of the impulse response. This result follows immediately by rewriting the expression of $e_{DAC,i}(t)$ from (24) as

$$e_{DAC,i}(t) = \Big\{ e_{hi}(t) + e_{li}(t) \Big\} \otimes c_i[n] + \sum_{n=-\infty}^{+\infty} \frac{e_{hi}(t-nT) - e_{li}(t-nT)}{2}, \quad (25)$$

where $c_i[n] \triangleq \big(b_i[n] - 1/2\big)$ is the 1-bit digital signal shifted to the zero-mean range $\{\pm 1/2\}$, and the convolution operation is explicitly marked with $\otimes$. The second term in (25) only contains harmonics at the multiples of the sampling frequency if $e_{hi}(t)$ and $e_{li}(t)$ differ from each other. By neglecting this term, the frequency-domain form of (25) becomes

$$E_{DAC,i}\big(f\big) = \Big\{ E_{hi}\big(f\big) + E_{li}\big(f\big) \Big\} \cdot C_i\big(f\big). \quad (26)$$

Hence, because $C_i\big(f\big)$ is shaped by the tree encoder described above, it follows that our system always "filters" the spectra of $e_{hi}(t)$ and $e_{li}(t)$ around the RX-band, regardless of their extension beyond $[0, T)$. Nevertheless, as the attenuation performance is limited by the instability problems mentioned earlier, the energy of the error pulses must be kept within reasonable bounds.

In conclusion, DEM can effectively correct all nonlinearities arising from static amplitude, timing, and pulse shape mismatches among different DAC conversion cells. On the other hand, this approach is ineffective against those nonlinearities arising from phenomena that are common to all conversion cells, such as the nonlinear output impedance in current-steering DACs. Fortunately, the relatively high immunity to mismatch problems enabled by DEM allows to specifically optimize the DAC with respect to these phenomena [21]. The many successful implementations of DEM realized over the years have undoubtedly demonstrated the performance advantage enabled by this technique. Last, it must be also mentioned that our solution does not take into consideration the possible nonlinearities introduced after the digital-to-analog conversion, for example if an external power amplifier (PA) is needed in the TX chain. The linearization of the PA response is a topic of its own, which is out of scope of this paper.

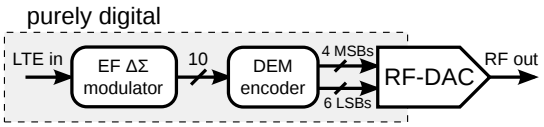

Fig. 10. Complete functional block diagram of the proposed solution.

IV. System-Level Simulations

In order to verify the validity of the proposed method, a system-level model of the $\Delta\Sigma$ DEM RF-DAC was created. The system block diagram is shown in Fig. 10. Both the $\Delta\Sigma$ modulator and DEM encoder implement the same programmable NTF given by (10). Similarly as in Section II, the RF-DAC has been modeled as an array of conversion cells with 10 bits of resolution, segmented into 4 unary-weighted MSBs and 6 binary-weighted LSBs. This segmentation choice represents a balanced trade-off between the total number of

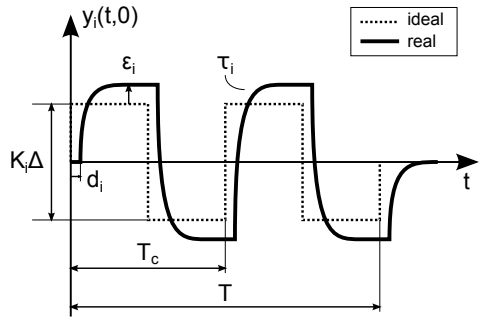

Fig. 11. Ideal and real impulse responses of a single differential RF-DAC conversion cell used in our system-level model.

switching blocks in the DEM encoder, the complexity of the RF-DAC circuitry, and the sensitivity to static mismatches [3].

The impulse response of each RF-DAC conversion cell is a waveform designed to fulfill (23). Fig. 11 plots the ideal and real responses for $n = 0$ and $b_i[0] = 1$. A differential implementation of the conversion cell is assumed, meaning that the waveforms with $b_i[0] = 0$ are the exact negation of those shown in Fig. 11. In order to avoid systematic glitches in the RF output, the sampling period of the digital input signal T should be a multiple of the carrier period T_c [4]. In Fig. 11, as well as in all simulations presented in the following, $T = 2T_c$ is assumed (i.e. the carrier frequency f_c is twice the digital sampling rate f_s). A configurable fractional interpolation chain that efficiently converts the base sampling rate of LTE signals to the gigahertz-range carrier-dependent sampling rate needed at the RF-DAC input has been published in [6].

The real impulse response differs from the ideal waveform in that it has finite rise and fall times defined by the time constant τ_i, is delayed by an amount d_i, and settles to an incorrect full-amplitude value determined by the amplitude error ε_i. These static parameters are used to model, respectively, the RC settling transient of the cell output, the nonzero propagation delay of the clock distribution network, and the inaccuracy of the circuitry determining the steady-state cell output value. Furthermore, note that the real waveform in Fig. 11 extends beyond the time window $[0, T)$.

Fig. 12(a) and (b) show the spectra of the analog output of the RF-DAC, when converting two LTE signals of bandwidths 20 and 15 MHz to E-UTRA bands 1 and 3 respectively [27]. Similarly as in Fig. 6, these spectra result from single simulation runs. Here, the delay mismatches d_i are taken from a Gaussian distribution with $\sigma_d = 0.05\%$ relative to T, resulting in a worst case cell-to-cell delay difference of a few picoseconds. The time constant of all cells in the LSB segment is $\tau_{LSB} = 3\%$ of T, whereas that of the MSB cells is 5% higher (i.e. $\tau_{MSB} = 1.05 \cdot \tau_{LSB}$). This models a nonlinear scaling of the cell drivers between the two segments. The amplitude mismatches ε_i are still modeled by (13), with $\sigma_{LSB} = 1\%$ relative to Δ. This value has been decreased compared to the simulation of Fig. 6, because now timing mismatches are also present. Nevertheless, in the authors' design experience, the chosen quantities are representative of the matching accuracy that can be achieved through careful analog design in current deep sub-micron CMOS technologies.

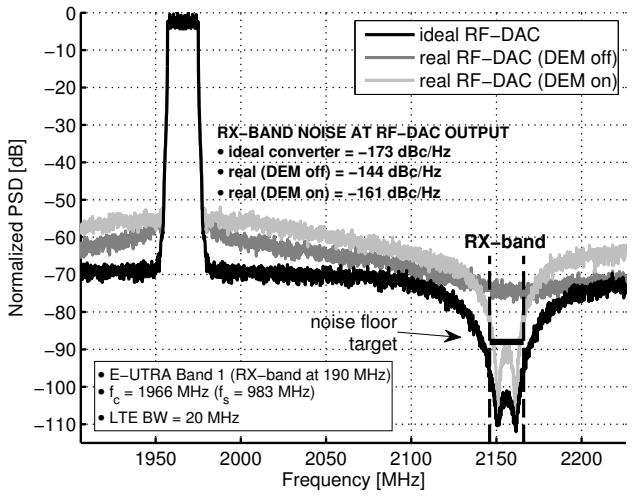

(a)

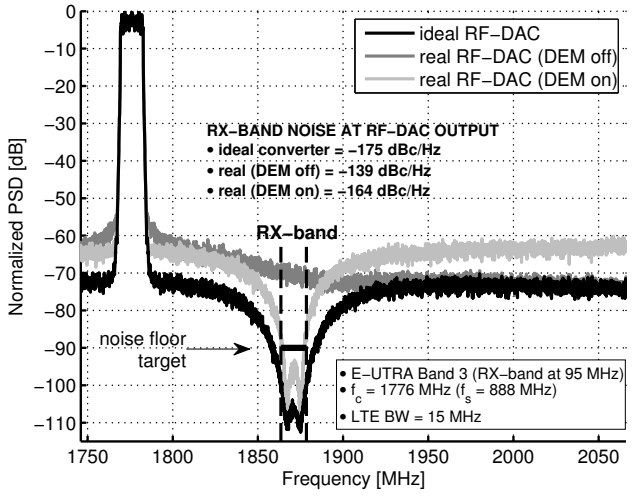

(b)

Fig. 12. Spectra of the signals at the output of the ideal RF-DAC, and the real RF-DAC with DEM activated and deactivated. Simulations with $\sigma_{LSB} = 1\%$, $\sigma_d = 0.05\%$, $\tau_{LSB} = 3\%$, and $\tau_{MSB} = 1.05 \cdot \tau_{LSB}$. The two simulations (a) and (b) are performed in different channel configurations, in order to highlight the flexibility of the $\Delta\Sigma$ DEM RF-DAC.

The simulations shown in Fig. 12 prove that DEM is capable of recovering the performance loss due to static DAC mismatches. Therefore, reducing the RX-band noise below –160 dBc/Hz is still possible without analog or semi-digital filtering. Note that, when DEM is activated, the shape of the spectral density follows closely that of the ideal signal, since the $\Delta\Sigma$ modulator and the switching sequence generators implement the same programmable NTF.

Similarly as in Section II, it has been verified that, with a pole radius of 0.8, the quality of the transmitted signal (in terms of ACLR and EVM) always remains well above the minimum LTE requirements. More importantly, the chosen pole radius also guarantees the stability of the sequence generation loops, thus demonstrating the feasibility of 4$^{\text{th}}$-order tunable DEM with a tree structure encoder. Even though only two tuning settings are shown here, the authors have checked that stable operation can be achieved for all possible band-

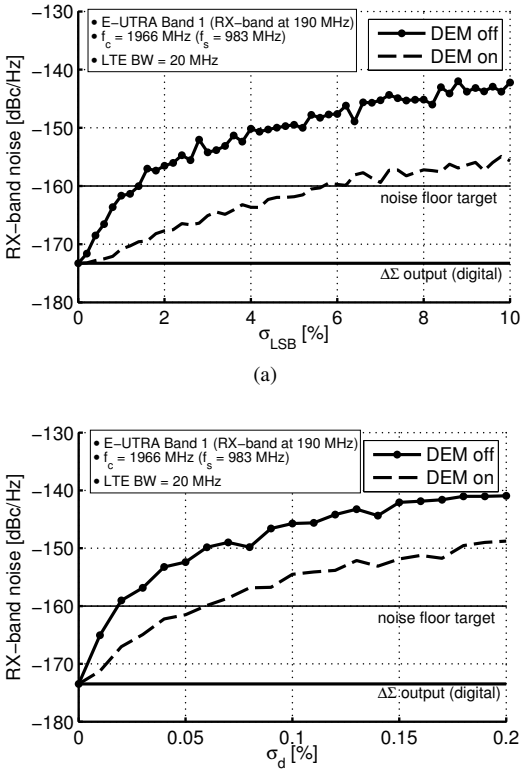

Fig. 13. Simulated RX-band noise as a function of the standard deviation of (a) the amplitude mismatch, and (b) the delay mismatch among different RF-DAC conversion cells, with all other nonidealities set to zero.

bandwidth combinations specified in the LTE standard.

Fig. 13(a) shows the dependence of the RX-band noise on the standard deviation of the amplitude mismatch, with no timing mismatches present. Likewise, Fig. 13(b) depicts the RX-band noise level when only delay mismatches are taken into consideration. Each point in the curves is averaged from 10 simulation runs. In both cases, for a given value of σ, activating DEM yields a $10 \sim 15$ dB improvement in the RX-band noise. Equivalently, DEM allows to meet a given noise target when the mismatch deviation is $3 \sim 5$ times larger. The performance improvement can be even larger when different mismatch sources are combined, as can be seen from the simulated noise levels in Fig. 12. Therefore, the combined effect of $\Delta\Sigma$ modulation and DEM boosts the RX-band noise performance considerably, without increasing at all the design effort of the analog circuitry.

The simulations presented above were performed with LTE signals of largest bandwidths (15 and 20 MHz). The bar graph of Fig. 14 illustrates the RX-band noise level for all six supported LTE bandwidths. This simulation was performed with the same mismatch scenario as in Fig. 12. Each bar results from the average of 10 simulation runs. The improvement brought by DEM grows remarkably with narrower bandwidths, as can be expected from the increase in oversampling ratio. This feature supports well frequency-division multiple access schemes such as LTE, because in most practical scenarios only a fraction of the total LTE bandwidth is assigned to a single user [28]. Hence, the NTF notches can be dynamically placed around the frequencies corresponding to the allocated band, thus further increasing the robustness of the transceiver.

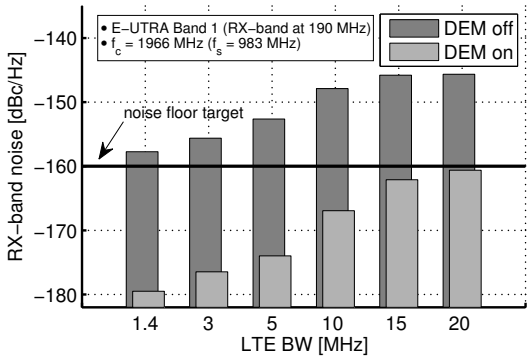

Fig. 14. Simulated RX-band noise as a function of the LTE channel bandwidth. The mismatch scenario is the same as in Fig. 12.

V. Conclusion

In this paper, a new approach to reduce the RX-band noise in all-digital transmitters was described. The proposed solution applies bandpass $\Delta\Sigma$ modulation and DEM to the RX-band instead of the transmit band, in order to shape the quantization and mismatch noise of the DAC. A method to design a highly flexible NTF was described, with emphasis on pole placement. The designed NTF enables stable 4^{th}-order tunable DEM with a tree structure encoder. Moreover, this paper presented a general analysis of DEM. The effectiveness of the proposed approach was verified through a number of accurate system-level simulations, showing a very good robustness against typical amplitude and timing DAC mismatches. Even though the simulations were performed in an LTE environment, the results would be equally valid in other FDD systems.

Unlike semi-digital methods, our fully digital approach inherits all the advantages of digital RF, such as simplification of the analog circuitry and relaxation of its performance requirements. Because the trend in RF IC design is to move to digitally-intensive architectures, our technique is a good candidate to reduce the filtering requirements at the TX output, eventually allowing to replace altogether the bulky and expensive SAW filters in the TX chain.

Acknowledgment

This work has been supported by Nokia Foundation.

References

[1] J. Vankka, J. Ketola, J. Sommarek, O. Vaananen, M. Kosunen, and K. A. I. Halonen, "A GSM/EDGE/WCDMA modulator with on-chip D/A converter for base stations," *IEEE Trans. Circuits Syst. II*, vol. 49, no. 10, pp. 645–655, Oct. 2002.

[2] M. Kosunen, J. Vankka, M. Waltari, and K. Halonen, "A multicarrier QAM modulator for WCDMA base-station with on-chip D/A converter," *IEEE Trans. VLSI Syst.*, vol. 13, no. 2, pp. 181–190, Feb. 2005.

[3] P. Eloranta, P. Seppinen, S. Kallioinen, T. Saarela, and A. Pärssinen, "A multimode transmitter in 0.13 μm CMOS using direct-digital RF modulator," *IEEE J. Solid-State Circuits*, vol. 42, no. 12, pp. 2774–2784, Dec. 2007.

[4] N. Zimmermann, B. Thiel, R. Negra, and S. Heinen, "System architecture of an RF-DAC based multistandard transmitter," in *52nd IEEE Int. Midwest Symp. Circuits and Systems*, Aug. 2009, pp. 248–251.

[5] Z. Boos, A. Menkhoff, F. Kuttner, M. Schimper, J. Moreira, H. Geltinger, T. Gossmann, P. Pfann, A. Belitzer, and T. Bauernfeind, "A fully digital multimode polar transmitter employing 17b RF DAC in 3G mode," in *IEEE Int. Solid-State Circuits Conf. Dig. Tech. Papers*, 2011, pp. 376–378.

[6] E. Roverato, M. Kosunen, J. Lemberg, T. Nieminen, K. Stadius, J. Ryynänen, P. Eloranta, R. Kaunisto, and A. Pärssinen, "A configurable sampling rate converter for all-digital 4G transmitters," in *21st European Conf. Circuit Theory and Design (ECCTD)*, Sep. 2013.

[7] S. Taleie, T. Copani, B. Bakkaloglu, and S. Kiaei, "A bandpass $\Delta\Sigma$ RF-DAC with embedded FIR reconstruction filter," in *IEEE Int. Solid-State Circuits Conf. Dig. Tech. Papers*, 2006, pp. 2370–2379.

[8] W. Gaber, P. Wambacq, J. Craninckx, and M. Ingels, "A CMOS IQ direct digital RF modulator with embedded RF FIR-based quantization noise filter," in *Proc. ESSCIRC*, 2011, pp. 139–142.

[9] S. Fukuda, S. Miya, M. Io, K. Hamashita, and B. Nauta, "Direct-digital modulation (DIDIMO) transmitter with –156dBc/Hz Rx-band noise using FIR structure," in *Proc. ESSCIRC*, 2012, pp. 53–56.

[10] M. Park, M. Perrott, and R. Staszewski, "An amplitude resolution improvement of an RF-DAC employing pulsewidth modulation," *IEEE Trans. Circuits Syst. I*, vol. 58, no. 11, pp. 2590–2603, Nov. 2011.

[11] J. Mehta, R. Staszewski, O. Eliezer, S. Rezeq, K. Waheed, M. Entezari, G. Feygin, S. Vemulapalli, V. Zoicas, C.-M. Hung, N. Barton, I. Bashir, K. Maggio, M. Frechette, M.-C. Lee, J. Wallberg, P. Cruise, and N. Yanduru, "A 0.8mm^2 all-digital SAW-less polar transmitter in 65nm EDGE SoC," in *IEEE Int. Solid-State Circuits Conf. Dig. Tech. Papers*, 2010, pp. 58–59.

[12] R. Schreier and G. C. Temes, *Understanding Delta-Sigma Data Converters*. Hoboken (NJ): Wiley, 2005.

[13] R. Schreier, "An empirical study of high-order single-bit delta-sigma modulators," *IEEE Trans. Circuits Syst. II*, vol. 40, no. 8, pp. 461–466, Aug. 1993.

[14] K.-H. Chao, S. Nadeem, W. Lee, and C. Sodini, "A higher order topology for interpolative modulators for oversampling A/D converters," *IEEE Trans. Circuits Syst.*, vol. 37, no. 3, pp. 309–318, Mar. 1990.

[15] T.-H. Kuo, K.-D. Chen, and J.-R. Chen, "Automatic coefficients design for high-order sigma-delta modulators," *IEEE Trans. Circuits Syst. II*, vol. 46, no. 1, pp. 6–15, Jan. 1999.

[16] M. Snoeij, O. Bajdechi, and J. Huijsing, "A 4th-order switched-capacitor sigma-delta A/D converter using a high-ripple Chebyshev loop filter," in *IEEE Int. Symp. Circuits and Systems (ISCAS)*, May 2001, pp. 615–618.

[17] Z.-M. Lin and W.-H. Sheu, "A generic multiple-feedback architecture and method for the design of high-order $\Sigma\Delta$ modulators," *IEEE Trans. Circuits Syst. II*, vol. 49, no. 7, pp. 465–473, Jul. 2002.

[18] J. Lindeberg, J. Vankka, J. Sommarek, and K. Halonen, "A 1.5-V direct digital synthesizer with tunable delta-sigma modulator in 0.13-μm CMOS," *IEEE J. Solid-State Circuits*, vol. 40, no. 9, pp. 1978–1982, Sep. 2005.

[19] I. Galton, "Spectral shaping of circuit errors in digital-to-analog converters," *IEEE Trans. Circuits Syst. II*, vol. 44, no. 10, pp. 808–817, Oct. 1997.

[20] T. Kaplan, J. Jensen, C. Fields, and M.-C. Chang, "A 2-GS/s 3-bit $\Delta\Sigma$-modulated DAC with tunable bandpass mismatch shaping," *IEEE J. Solid-State Circuits*, vol. 40, no. 3, pp. 603–610, Mar. 2005.

[21] K. L. Chan and I. Galton, "A 14b 100MS/s DAC with fully segmented dynamic element matching," in *IEEE Int. Solid-State Circuits Conf. Dig. Tech. Papers*, 2006, pp. 2390–2399.

[22] K. L. Chan, J. Zhu, and I. Galton, "A 150MS/s 14-bit segmented DEM DAC with greater than 83dB of SFDR across the Nyquist band," in *IEEE Symp. VLSI Circuits*, Jun. 2007, pp. 200–201.

[23] K. L. Chan, N. Rakuljic, and I. Galton, "Segmented dynamic element matching for high-resolution digital-to-analog conversion," *IEEE Trans. Circuits Syst. I*, vol. 55, no. 11, pp. 3383–3392, Dec. 2008.

[24] I. Galton, "Why dynamic-element-matching DACs work," *IEEE Trans. Circuits Syst. II*, vol. 57, no. 2, pp. 69–74, Feb. 2010.

[25] N. Sun, "High-order mismatch-shaping in multibit DACs," *IEEE Trans. Circuits Syst. II*, vol. 58, no. 6, pp. 346–350, Jun. 2011.

[26] ——, "High-order mismatch-shaped segmented multibit $\Delta\Sigma$ DACs with arbitrary unit weights," *IEEE Trans. Circuits Syst. I*, vol. 59, no. 2, pp. 295–304, Feb. 2012.

[27] *User Equipment (UE) radio transmission and reception*, 3GPP Std. TS 36.101, Rev. 12.2.0, Dec. 2013.

[28] O. Oliaei, M. Kirschenmann, D. Newman, K. Hausmann, H. Xie, P. Rakers, M. Rahman, M. Gomez, C. Yu, B. Gilsdorf, and K. Sakamoto, "A multiband multimode transmitter without driver amplifier," in *IEEE Int. Solid-State Circuits Conf. Dig. Tech. Papers*, 2012, pp. 164–166.

Enrico Roverato (S'13) was born in Padova, Italy, in 1988. He received the B.Sc. degree in information engineering from University of Padova, in 2010, and the M.Sc. degree in electrical engineering from Aalto University, Espoo, Finland, in 2012. He is currently a researcher at Aalto University, Department of Micro- and Nanosciences, where he is working towards the Ph.D. degree. His research interests are on all-digital RF transmitter circuits, with special focus on the implementation of high-speed DSP algorithms.

Marko Kosunen (S'97–M'07) received his M.Sc, L.Sc and D.Sc (with honors) degrees from Helsinki University of Technology, Espoo, Finland, in 1998, 2001 and 2006, respectively. He is currently a Senior Researcher at Aalto University, Department of Micro and Nanosciences. His expertise is in implementation of the wireless transceiver DSP algorithms and communication circuits. He is currently working on cognitive radio spectrum sensors, energy autonomus wireless sensor nodes, digital intensive transceiver circuits and medical sensor electronics.

Jerry Lemberg was born in Lohja, Finland, in 1986. He received the Master of Science degree in electrical engineering from Aalto University, Espoo, Finland, in 2013. He is currently pursuing the Doctoral degree at the School of Electrical Engineering, Aalto University. His research interests include high-speed digital-to-analog converters and digital intensive transmitters.

Kari Stadius (S'95–M'03) received the M.Sc., Lic. Tech., and Doctor of Science degrees in electrical engineering from the Helsinki University of Technology, Helsinki, Finland, in 1994, 1997, and 2010, respectively. He is currently working as a research scientist at the Department of Micro- and Nanosciences, Aalto University School of Electrical Engineering. His research interests include the design and analysis of RF transceiver blocks with special emphasis on frequency synthesis, and new emerging RF technologies such as graphene. He has authored or coauthored over 70 refereed journal and conference papers in the areas of analog and RF circuit design.

Jussi Ryynänen (S'99–M'04) was born in Ilmajoki, Finland, in 1973. He received the Master of Science and Doctor of Science degrees in electrical engineering from the Helsinki University of Technology (HUT), Helsinki, Finland, in 1998, and 2004, respectively. He is currently a Professor in the Department of Micro- and Nanosciences, Aalto University School of Electrical Engineering. His main research interests are on integrated transceiver circuits for wireless applications. He has authored or coauthored over 100 refereed journal and conference papers in the areas of analog and RF circuit design. He holds several patents on RF circuits. He is currently a member of the technical program committee of the IEEE International Solid-State Circuits Conference and IEEE European Solid-State Circuits Conference.